RAA 2019 Vol. **19** No. **9**, 123(8pp) doi: 10.1088/1674–4527/19/9/123

http://www.raa-journal.org *http://iopscience.iop.org/raa*

Research in Astronomy and Astrophysics

Design and on-orbit status of the trigger system for the DAMPE mission

Yong-Qiang Zhang[1,2⋆], Jian-Hua Guo[1⋆], Yang Liu[1], Chang-Qing Feng[3], Yun-Long Zhang[3], Tie-Kuang Dong[1], Jing-Jing Zang[1] and Chuan Yue[1]

[1] Key Laboratory of Dark Matter and Space Astronomy, Purple Mountain Observatory, Chinese Academy of Sciences, Nanjing 210008, China; *zhangyq@pmo.ac.cn, jhguo@pmo.ac.cn*

[2] University of Chinese Academy of Sciences, Beijing 100049, China

[3] State Key Laboratory of Particle Detection and Electronics, University of Science and Technology of China, Hefei 230026, China

Received 2018 December 19; accepted 2019 March 18

Abstract DArk Matter Particle Explorer (DAMPE), the first Chinese astronomical satellite, was successfully launched at the Jiuquan Satellite Launch Center on 2015 Dec. 17. DAMPE consists of four subdetectors: Plastic Scintillator array Detector (PSD), Silicon-Tungsten tracKer-converter (STK), Bismuth Germanium Oxide (BGO) imaging calorimeter and NeUtron Detector (NUD). The global hardware trigger signal, which is generated by hits from the BGO calorimeter and the trigger logic board in the data acquisition system (DAQ), is responsible for event selection and DAQ synchronization of DAMPE. On orbit, to improve the detection efficiency, different trigger logics are used for event selection in different regions of latitude. The DAMPE trigger system compresses the average on-orbit trigger rate to 60 Hz and reduces science data mass to less than 13 GB per day to meet the requirement for the satellite's data link. The whole trigger system has run stably up to now, ensuring excellent on-orbit operation of DAMPE.

Key words: Dark Matter — instrumentation: detectors — methods: data analysis

1 INTRODUCTION

The DArk Matter Particle Explorer (DAMPE) is a space-based mission designed as a high energy particle detector measuring cosmic rays and γ-rays (Chang et al. 2014; Chang et al. 2017). The wide dynamical range of energy measurement (5 GeV−10 TeV for electrons/positrons and γ-rays), good energy resolution (1.5% @ 800 GeV for electrons/positrons and γ-rays), and powerful particle identification (PID) capability, make DAMPE one of the most sensitive detectors for indirect detection of dark matter (DAMPE Collaboration et al. 2017; Yuan & Feng 2018). The scientific payload of DAMPE is composed of a Plastic Scintillator array Detector (PSD), a Silicon-Tungsten tracKer-converter (STK), a Bismuth Germanium Oxide (BGO) imaging calorimeter and a NeUtron Detector (NUD). The PSD is designed to measure the charges of incident particles up to $Z = 28$ (Zhou et al. 2016; Yu et al. 2017; Ding et al. 2019; Ma et al. 2018; Dong et al. 2019), and rejects charged-particle background for γ-rays (Xu et al. 2018). The STK measures the trajectories and also the charges of incident particles (Azzarello et al. 2016; Qiao et al. 2018), and provides electron/gamma discrimination. The BGO calorimeter, which is designed as a total-absorption electromagnetic calorimeter with about 32 radiation lengths, precisely measures the energy of incident particles and facilitates efficient electron/hadron identification (Zhang et al. 2016a; Wei et al. 2016). The NUD provides further improvement for electron/hadron identification (He et al. 2016). DAMPE utilizes a global hardware trigger signal to select events of interest and synchronize the data acquisition system (DAQ) (Chang et al. 2009; Guo et al. 2012; Zhang et al. 2012; Zhang et al. 2017; Ambrosi et al. 2019).

As is well known, most cosmic rays in the GeV-TeV range are protons, alpha particles and heavier nuclei, while electrons/positrons and γ-rays account for less than 1%. However, for DAMPE, electrons/positrons and γ-rays are the most important target particles for indirect detection of dark matter. Based on the different distribution of energy depositions in the BGO calorimeter due to electromagnetic

⋆ Corresponding author.

and hadronic showers, the trigger system is designed to reject hadron backgrounds and enlarge the acceptance of target particles as much as possible. The trigger system of DAMPE is based on the joint work of the BGO calorimeter and trigger board. When the deposited energy in a BGO bar exceeds the threshold of the comparator, the hit signal is sent to the trigger board in the DAQ crate. Also, if the hit signals from the BGO calorimeter match the trigger logics, the trigger board generates a trigger signal and sends it to the DAQ system. This paper will introduce the design of the trigger system and the trigger threshold calibration, as well as the on-orbit status of the trigger system.

2 THE TRIGGER SYSTEM OF DAMPE

2.1 The Trigger and Data Acquisition System

In DAMPE, the front-end electronics (FEEs) of the detector are used for signal readout and digitization. The DAQ system mainly consists of two electronic crates, the Payload Data Processing Unit (PDPU) and the Payload Management Unit (PMU). The PDPU distributes commands to the FEEs on the $+X/+Y$ side, collecting housekeeping data and science data from them. The PMU applies the same process to FEEs on the $-X/-Y$ side. All collected data are finally stored in the PMU, which has a memory of $\sim$16 GB. A detailed introduction to the DAQ system has been described in Chang et al. (2017).

Figure 1 illustrates a schematic diagram of the trigger and DAQ system for DAMPE. For an incident particle, the hit signals from the BGO calorimeter are transferred to the trigger system that checks if the trigger logic is satisfied. After the trigger decision, the trigger system sends an effective trigger signal to the FEEs of each sub-detector and the DAQ system simultaneously. The FEEs will delay the trigger signal and latch the peak value of the integral signal, i.e. the so-called signal digitization. After the digitization process, the FEEs pack the data with zero-suppression and send them to the PDPU/PMU, which packs the received data and adds some necessary tags, e.g. a time stamp. Finally, the PMU transfers the scientific data in CCSDS format to ground stations.

2.2 Hit Generation in the BGO Calorimeter

Figure 2 shows the layout of the BGO calorimeter. The BGO calorimeter consists of 308 BGO crystal bars, and the size of each one is 2.5 cm$\times$2.5 cm$\times$60 cm. All the bars are stacked in a hodoscopic configuration of 14 layers, with 22 BGO crystals in each layer, to achieve a longitudinal depth of $\sim$32 radiation lengths.

To satisfy the requirement of energy measurement with a large dynamic range of about 10^6 for each BGO crystal, a photomultiplier tube (PMT)-based multi-dynode readout scheme is implemented (Zhang et al. 2012; Feng et al. 2015). As shown in Figure 3, each BGO bar is read out by two Hamamatsu R5610A-01 PMTs on both sides. The PMTs are coupled to the crystals with optical attenuators, which attenuate the scintillation light produced in the BGO crystal to adjust the PMT response to the deposited energy. The signals of three dynodes dy2, dy5 and dy8, corresponding to a low-gain channel, a medium-gain channel and a high-gain channel respectively, are picked up by the charge measurement ASIC, VATA160 (Ideas 2013), which is manufactured by the IDEAS company.

VATA160 is mainly composed of two parts: a charge measurement part called VA and a hit signal generation part called TA. The VA part of VATA160 has 32 analog input channels and each channel consists of a charge-sensitive pre-amplifier (CSA), a CR-RC shaping amplifier and a sample and hold circuit (SH); the TA part for each channel has a fast shaper and a comparator. After being pre-amplified in VA, each signal from the PMT dynodes is split and distributed to both the VA part and the TA part. The signals to the TA part are shaped with the faster shaper and then discriminated by the comparators with pre-configured threshold voltage level. All the 32 outputs of the TA part are OR-ed together and a hit signal is generated.

In the BGO calorimeter, the signals from the same dynodes from the same side of 22 BGO bars in one layer are connected to one VA160, as illustrated in Figure 4. On orbit, only signals from the dyn8 and dyn5 of PMTs in the top four layers (Layer1$\sim$Layer4) and bottom four layers (Layer11$\sim$Layer14) are employed for hit signal generation.

2.3 Trigger Logic Design

The trigger decision is implemented by a Printed Circuit Board (PCB) as Figure 5 depicts, which is located in the PDPU crate. The trigger board utilizes an FPGA (APA300) chip to produce the trigger decision. The trigger logic scheme is displayed in Figure 6. There are three different trigger patterns in DAMPE, i.e., an external trigger, a periodical trigger and an event trigger. The external trigger is used for ground tests before launch. The periodical trigger, which generates a specified number of events with a particular rate, is used for pedestal calibration and linearity calibration in electronics. The event trigger is configured to acquire the scientific data. DAMPE trigger signals are generated by the logical “OR” of the outputs from these three trigger patterns.

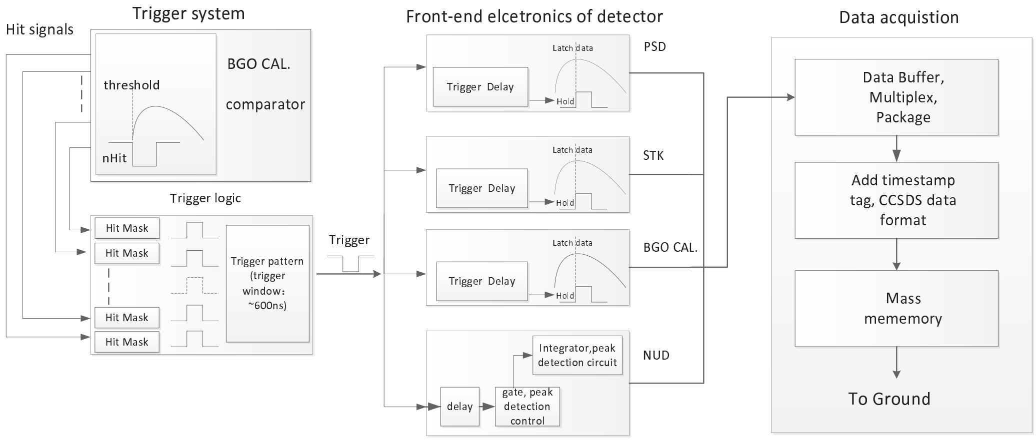

Fig. 1 The trigger and DAQ system of DAMPE.

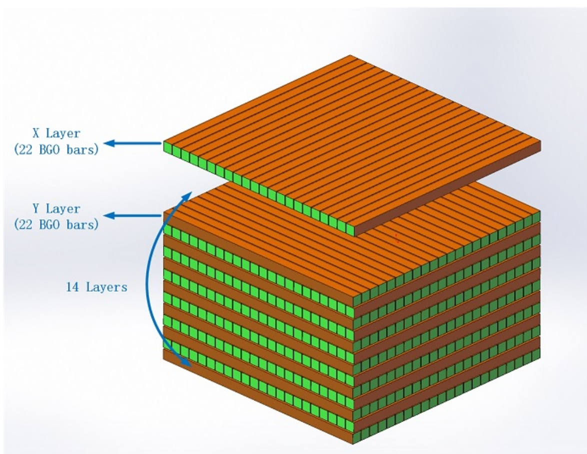

Fig. 2 Schematic view of the BGO calorimeter.

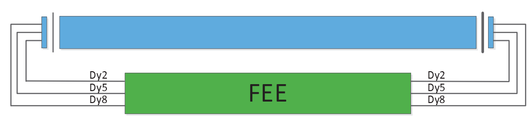

Fig. 3 Readout of a BGO bar.

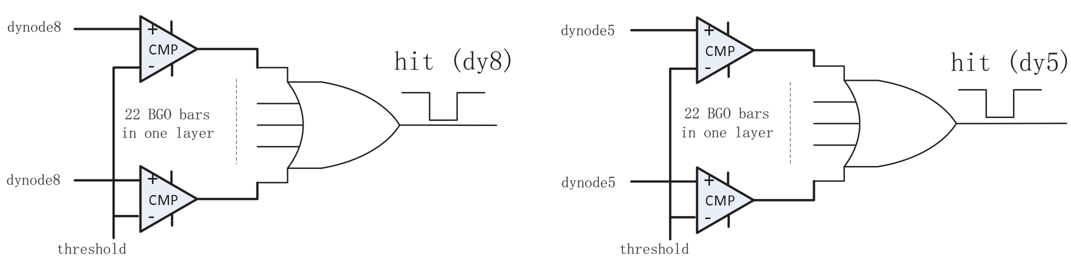

Fig. 4 Hit generation.

For the event trigger pattern, there are four kinds of trigger engines, i.e., unbiased trigger, minimum ionizing particles (MIPs) trigger, high energy trigger and low energy trigger, and its configuration on orbit is shown in Table 1. The hit signal from dyn8 channels of the first layer on the positive side is abbreviated as L1_P8, and so forth.

Unbiased triggers, as shown in Table 1, with very low thresholds of ∼0.4 MIPs (the energy deposition of MIPs in one BGO bar, which is about 23 MeV (Zhang et al. 2016b)) in the top two BGO layers ensure the trigger efficiency to high energy electrons/γ-rays (>5 GeV) is nearly 100%, and can be used to calibrate the trigger efficiency for high energy triggers. On the other hand, this trigger engine can monitor the flux variation of cosmic rays in different space zones.

The MIPs trigger is mainly used to choose the MIPs (protons in most cases) that penetrate the whole calorimeter from the top layer to the bottom layer without an ac-

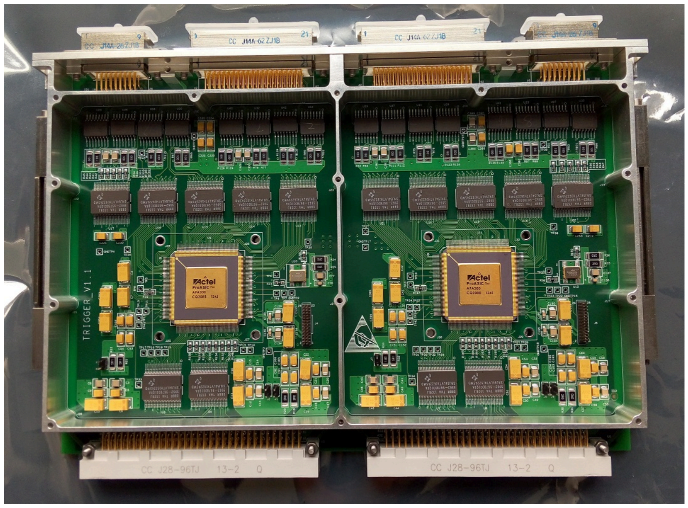

Fig. 5 Trigger board.

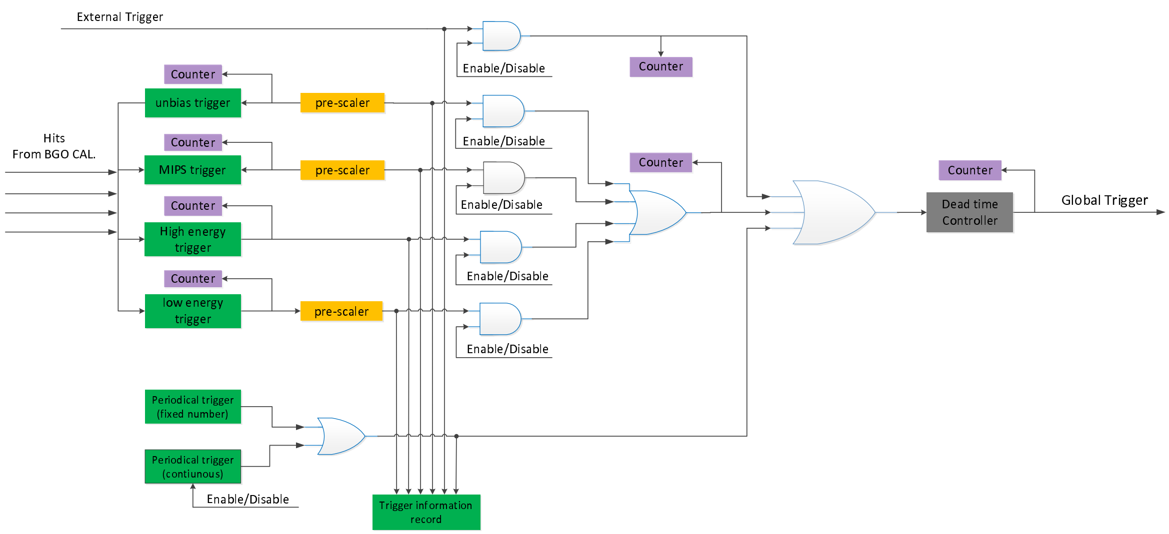

Fig. 6 The trigger logic scheme of DAMPE.

Table 1 On-orbit Configuration of Trigger System

Trigger engine	Trigger logic	Trigger threshold (MIPs)	Comment
Unbiased trigger	(L1_P8 & L1_N8) | (L2_P8 & L2_N8)	L1_P8: 0.4; L1_N8: 0.4; L2_P8: 0.4; L2_N8: 0.4	
MIPs trigger	(L3_P8 & L11_P8 & L13_P8) | (L4_P8 & L12_P8 & L14_P8)	L3_P8: 0.4; L11_P8: 0.4; L13_P8: 0.4; L4_P8: 0.4; L12_P8: 0.4; L14_P8: 0.4	Proton/He: penetrate the whole BGO
High energy trigger	L1_P5 & L2_P5 & L3_P5 & L4_N8	L1_P5: 10; L2_P5: 10; L3_P5 : 10; L4_N8: 2	Electron/gamma >5 GeV
Low energy trigger	L1_N8 & L2_N8 & L3_N8 & L4_N8	L1_N8: 0.4; L2_N8: 0.4; L3_N8 : 2; L4_N8: 2	Electron/gamma >1 GeV

companying shower and deposit minimum ionizing energy in the BGO bars. As the energy deposition from a minimum ionizing particle passing through a BGO bar (25 mm-thick) is fixed at about 23 MeV by ionization, MIPs trigger events are used for energy calibration of the BGO calorimeter on orbit. To achieve this purpose, the trigger logic is set as (L3_P8 & L11_P8 & L13_P8) | (L4_P8 & L12_P8 & L14_P8) to guarantee the particles selected penetrate the whole calorimeter, and the thresholds of these layers are set to $\sim$0.4 MIPs.

The electrons/γ-rays passing through the BGO calorimeter induce good shower-development before or in its top layers, and the protons tend to create showers in the later layers. Based on this, the high energy trigger, the most important trigger engine for high energy electron/γ-ray selection, requires high energy thresholds in the top BGO layers. And so, the trigger logic is set as the first four layers AND-ed together with higher thresholds as shown in Table 1.

The low energy trigger is used to select the low energy electrons/γ-rays. The trigger logic is set as the first four layers AND-ed together with lower thresholds as shown in Table 1.

On orbit, the unbiased trigger, MIPs trigger and low energy trigger are pre-scaled to limit the global trigger rate.

The timing of the trigger decision procedure is displayed in Figure 7. To avoid jitter in the trigger signals from different events, DAMPE uses a low threshold hit signal T0 as the timing reference to open a coincidence window before a trigger decision is made. All the hit signals are recorded with a 25 ns period clock. The general width of hit signals is 1000 ns. The maximum skew of different hit signals is about 400 ns (Gao et al. 2014). The trigger window is configurable and optimized to 600 ns to ensure full timing redundancy and high efficiency. Once the T0 signal initiates the trigger decision procedure, DAMPE enables different trigger engines at the same time. DAMPE latches the coincidence results in the middle and at the end of the trigger coincidence window. As long as one of these two results is valid, DAMPE would send an effective trigger to all detectors to acquire data.

3 ON-ORBIT STATUS OF THE TRIGGER SYSTEM

3.1 Trigger Threshold Calibration

When the output signal of one dynode channel in the TA part of VATA160 exceeds the trigger threshold, its hit information would be sent to the trigger system for a trigger decision. To calibrate the threshold of each channel, the fired dynode channel in each BGO layer must be obtained based on the trigger information of each event. In a BGO layer, if only one dynode channel with the largest analog-to-digital converter (ADC) value exceeds the threshold while the other channels are regarded as noise channels, then this channel must be the fired channel for the trigger decision. From the flight data, we can obtain the ADC distribution for such a fired dynode channel, which can be used to calculate the corresponding threshold for this channel. In such an ADC distribution, the counts next to the threshold would manifest a sharp decrease, like a “cut off,” as exhibited in Figure 8(a). The sharply decreasing slope is called a “cut off” zone. Here we calculate the ADC value at the center of the slope where the count is half of the maximum count, as the ADC threshold for this dynode channel. In DAMPE, all the channels in a VATA160 share a configurable threshold. However, different channels, which include a VA and TA readout circuit, have different responses to input dynode signals, so the threshold must be calibrated channel by channel.

Table 2 The Trigger Threshold Calibration Result On Orbit

Hit signal	Average threshold (MIPs)	Hit signal	Average threshold (MIPs)
L1_P8	0.23	L4_P8	0.25
L1_N8	0.23	L4_N8	2.40
L1_P5	12.84	L11_P8	0.25
L2_P8	0.22	L12_P8	0.24
L2_N8	0.21	L13_P8	0.25
L2_P5	15.12	L14_P8	0.21
L3_P8	0.25		
L3_N8	2.24		
L3_P5	12.93		

Figure 8(a) plots a typical ADC distribution of a fired dynode channel with its “cut off” zone and the calculated threshold; Figure 8(b) depicts the threshold distribution of dyn5 in the first layer of the BGO calorimeter. It can be found that the variation of the threshold for different channels is less than 25 ADC bins.

Based on the MIPs calibration and the dynode linearity calibration (Zhang et al. 2016b), the trigger threshold in ADC units can be converted to energy units, as shown in Table 2. The average threshold is the mean value of the dynode channels on the same side in one BGO layer.

3.2 The Trigger Threshold’s Stability

DAMPE will operate on orbit for more than 3 years, and stability of the trigger threshold is very important and must be investigated carefully. To monitor the fluctuation of the trigger threshold, the calibration is carried out every day with data from the latest 5 days. A typical curve of the trigger threshold fluctuation versus time is displayed in Figure 9.

It can be found that fluctuation of the trigger threshold has a negative correlation with temperature, about -1.4 ADC bins per degree Centigrade (see Fig. 10), and the relationship has been very stable over the past 35 months. The negative correlation might be caused by the charge measurement ASIC (Zhang et al. 2016a), and further analysis is under consideration.

3.3 Trigger Rate

Each trigger engine has an individual counter to monitor its trigger rate. Figure 11 depicts the trigger rate distributions of the four engines versus latitude and longitude.

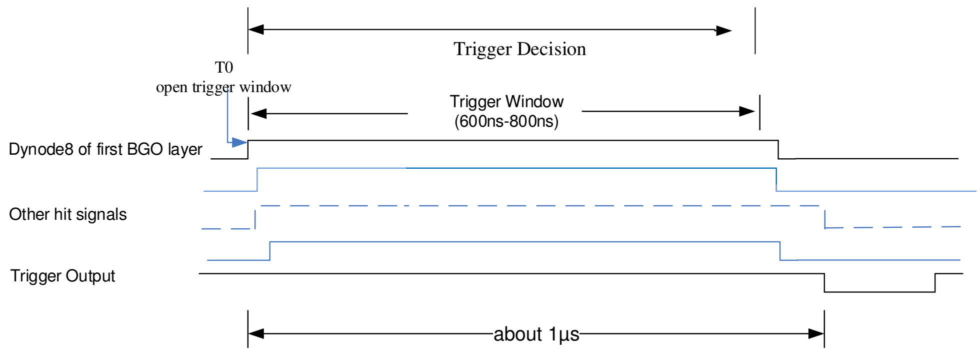

Fig. 7 The timing of a trigger decision.

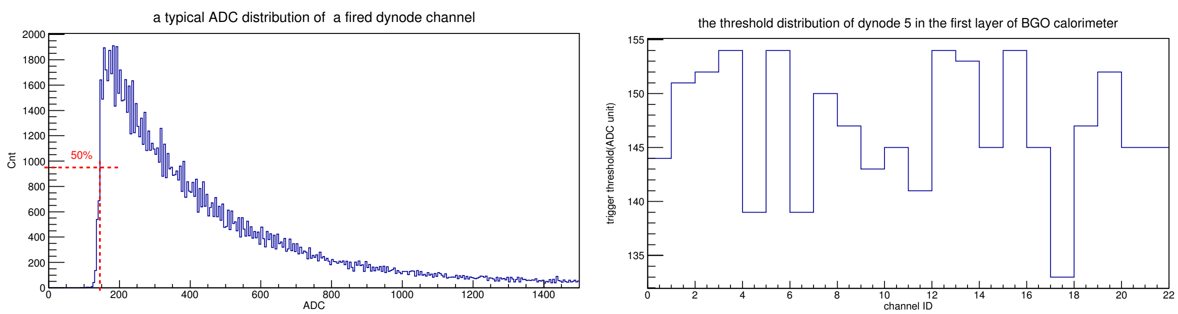

Fig. 8 Trigger threshold calibration result.

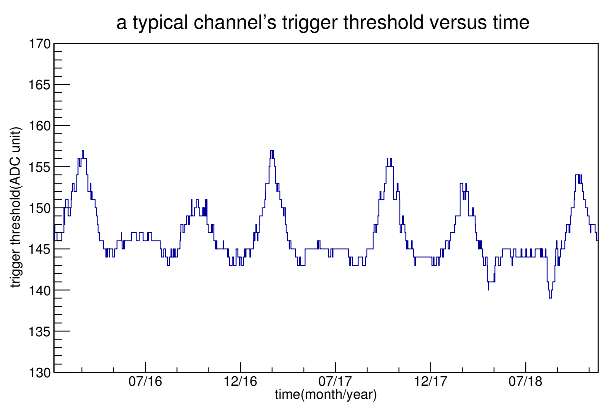

Fig. 9 Fluctuation of the threshold versus time.

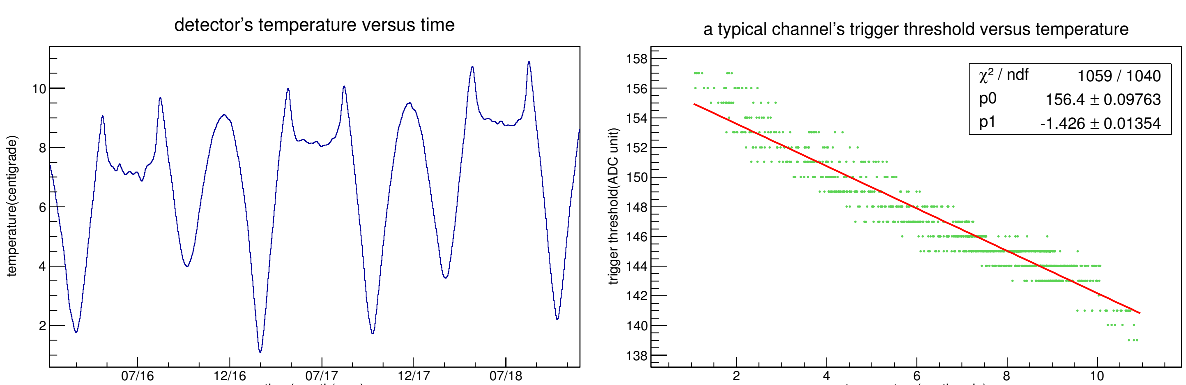

Fig. 10 The relationship between trigger threshold and temperature.

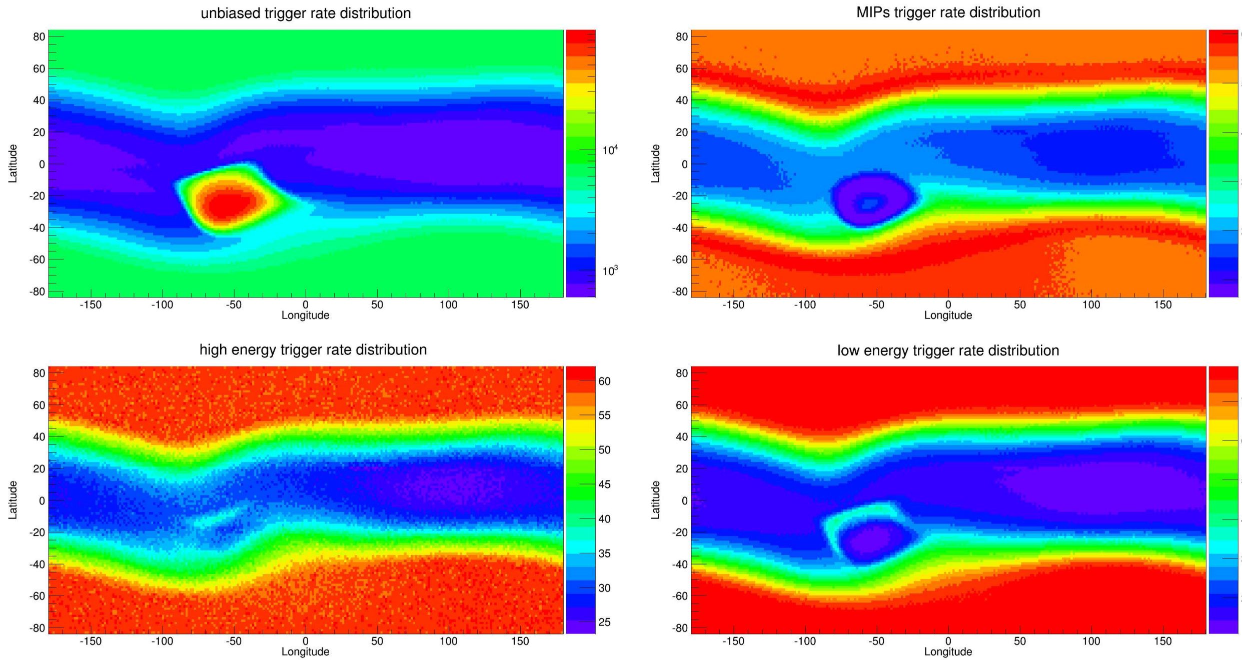

Fig. 11 Trigger rate distributions of the trigger engines.

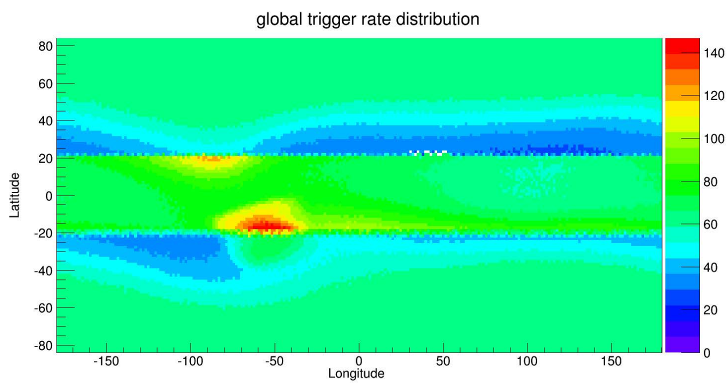

Fig. 12 Global trigger rate distribution.

Table 3 Operation On Orbit

Trigger engine	Enable/disable	Pre-scale	Trigger rate pre-scaled
Unbiased trigger	Enable	Latitude in $(-20, +20)$: 512; Others: 2048	$\sim$2 Hz
MIPs trigger	Latitude in $(-20, +20)$: enable; Others: disable	Latitude in $(-20, +20)$: 4	$\sim$40 Hz
High energy trigger	Enable	Not pre-scaled	40 Hz$\sim$60 Hz
Low energy trigger	Enable	Latitude in $(-20, +20)$: 8; Others: 64	10 Hz$\sim$20 Hz

In low latitudes and high latitudes, the unbiased trigger rate is $\sim$1 kHz and $\sim$10 kHz, respectively, while in the South Atlantic Anomaly (SAA) region it can reach as high as 100 kHz. The flux of cosmic rays in the SAA region is so high that performance of the electronics, including pedestal and dynode linearity, would be influenced, and therefore detector data acquired in the SAA are not used for scientific analysis. As a matter of fact, the unbiased trigger rate is utilized to identify times when DAMPE crosses the SAA.

As shown in Figure 11, outside the SAA region, the trigger rate of each trigger engine is mainly affected by the polar radiation zone. The dead time of the DAQ is fixed at 3.0725 ms. Therefore, in order to enlarge the detection efficiency for high-energy particles, it is necessary to pre-scale the other trigger engines except the high energy trigger. Based on the observational requirement and cosmic ray flux variation with latitude, the three trigger engines are pre-scaled as shown in Table 3. In the low latitude region ($-20\sim 20$), the unbiased trigger, MIPs trigger and low energy trigger are pre-scaled by factors 1/512, 1/4 and 1/8 respectively. In high latitudes, the MIPs trigger is disabled, and the pre-scale values of the unbiased trigger and low energy trigger are set to 1/2048 and 1/64 respectively.

After pre-scaling, the unbiased trigger rate is about 2 Hz except in the SAA region, the MIPs trigger rate is about 40 Hz in the low latitude region, the high energy trigger rate is about $40 \sim 60$ Hz and the low energy trigger rate is about $10 \sim 20$ Hz. The global trigger rate distribution with latitude and longitude is shown in Figure 12. The trigger rate is limited to less than 100 Hz in most areas, which could satisfy the detection requirements for high energy electron/γ-rays and relieve pressure on data transmission as well.

4 CONCLUSIONS

DAMPE has been operating on orbit very well for more than 35 months, and has successfully recorded more than five billion high-energy particle events. On orbit, the trigger system of DAMPE applies four different trigger engines, i.e., the unbiased trigger, MIPs trigger, high energy trigger and low energy trigger, for different requirements. The trigger thresholds are calibrated carefully with flight data and it is found that the trigger threshold shows a negative correlation with temperature. The global trigger rate is less than 100 Hz in most regions with the application of a pre-scaler, which ensures detection efficiency for high energy particles and also reduces data transmission pressure of the satellite platform effectively.

Acknowledgements In China, this work is supported in part by the National Key Research and Development Program of China (2016YFA0400201), the National Natural Science Foundation of China (Grant Nos. 11622327, 11273070, 11673075, U1738205, U1738121, U1738207, U1531126, 11873021 and 11773085), the Youth Innovation Promotion Association of the Chinese Academy of Sciences (No. 2014275) and the Space Science Mission Concept Research of Strategic Priority Research Program in Space Science of Chinese Academy of Sciences (No. XDA 15007114).

In Europe the activities and data analysis are supported by the Swiss National Science Foundation (SNSF), Switzerland, and the National Institute for Nuclear Physics (INFN), Italy.

References

Azzarello, P., Ambrosi, G., Asfandiyarov, R., et al. 2016, Nuclear Instruments and Methods in Physics Research A, 831, 378
Chang, J., & Wu, J. 2009, in Proc. 31st International Cosmic Ray Conf., 1, 1613
Chang, J. 2014, Chin. J. Spac. Sci., 34, 550
Chang, J., Ambrosi, G., An, Q., et al. 2017, Astroparticle Physics, 95, 6
DAMPE Collaboration, Ambrosi, G., An, Q., et al. 2017, Nature, 552, 63
DAMPE collaboration Ambrosi, G., An, Q., et al. 2019, Astroparticle Physics, 106, 18
Ding, M., Zhang, Y.-P., Zhang, Y.-J., et al. 2019, RAA (Research in Astronomy and Astrophysics), 19, 047
Dong, T., Zhang, Y., Ma, P., et al. 2019, Astroparticle Physics, 105, 31
Feng, C., Zhang, D., Zhang, J., et al. 2015, IEEE Transactions on Nuclear Science, 62, 3117
Gao, S. S., et al. 2014, in Proc. 19th IEEE Real-Time Conf., 1, 1.
Guo, J.-H., Cai, M.-S., Hu, Y.-M., & Chang, J. 2012, Chinese Astronomy and Astrophysics, 36, 318
He, M., Ma, T., Chang, J., et al. 2016, Acta Astronomica Sinica, 57, 1
VATA160 datasheet, 2013, Integrated Detector Electronics AS (IDE AS), Oslo, Norway, [Online]. Available: `http://www.ideas.no`
Ma, P.-X., Zhang, Y.-J., Zhang, Y.-P., et al. 2018, arXiv:1808.05720
Qiao, R., Peng, W.-X., Guo, D.-Y., et al. 2018, Nuclear Instruments and Methods in Physics Research A, 886, 48
Wei, Y., Zhang, Z., Zhang, Y., et al. 2016, IEEE Transactions on Nuclear Science, 63, 548
Xu, Z.-L., Duan, K.-K., Shen, Z.-Q., et al. 2018, RAA (Research in Astronomy and Astrophysics), 18, 027
Yu, Y., Sun, Z., Su, H., et al. 2017, Astroparticle Physics, 94, 1
Yuan, Q., & Feng, L. 2018, Science China Physics, Mechanics, and Astronomy, 61, 101002
Zhang, Y.-L., Li, B., Feng, C.-Q., et al. 2012, Chinese Physics C, 36, 71
Zhang D. L. et al., 2016a, Chin. Phys. C, 40, 145
Zhang, Z., Wang, C., Dong, J., et al. 2016b, Nuclear Instruments and Methods in Physics Research A, 836, 98
Zhang, Y. Q. , Liu, Y., & Guo, J. H. 2017, in Proc. 35th International Cosmic Ray Conf., 1, 232
Zhou, Y., Sun, Z., Yu, Y., et al. 2016, Nuclear Instruments and Methods in Physics Research A, 827, 79